https://doi.org/10.1016/j.jpowsour.2021.230538

A hybrid system integrating solid oxide fuel cell and thermo-radiative-photovoltaic cells for energy cascade utilization

Tianjun Liao[a, b], Yawen Dai[a], Chun Cheng[a], Qijiao He[a], Zheng Li[a], Meng Ni[a*]

[a] *Department of Building and Real Estate, Research Institute for Sustainable Urban Development (RISUD) and Research Institute for Smart Energy (RISE), Hong Kong Polytechnic University, Hung Hom, Kowloon, Hong Kong, China*

[b] *Department of Physics and Energy, Chongqing University of Technology, Chongqing 400054, China*

Abstract: A novel hybrid system coupling solid oxide fuel cell (SOFC) with thermoradiative (TR) and photovoltaic (PV) cells is proposed, evaluated, and optimized for energy cascade utilization. Theories of electrochemistry, Planck radiative heat transfer, and first law of thermodynamics are applied to assess and optimize the performance of the hybrid system. Firstly, energy balance analysis is conducted to obtain suitable area ratio between the subsystems and the SOFC. A homo-structure InAs-InAs is chosen as an example of the TP-PV cells. The peak power density of 0.669 $W \cdot cm^{-2}$ and the maximum efficiency of 0.770 and the relevant work conditions are achieved through parametric optimal analysis. It is also found that decreasing the leakage resistance of the SOFC can enhance electricity production and efficiency of the hybrid system. Secondly, a GaSb-InSb TP-PV cells are adopted to couple with the SOFC for performance enhancement. Finally, the positive effects of back surface reflector and the negative effects of irreversible heat transfers on the hybrid system are discussed. The obtained results are helpful for designing and optimizing the SOFC-TR-PV hybrid systems.

Key words: Solid oxide fuel cell; Thermoradiative cell; Thermophotovoltaic cell; Waste heat recovery; Energy cascade utilization.

*Corresponding author (M. Ni)
Email: meng.ni@polyu.edu.hk; Tel: 852-27664152; Fax: 852-27645131 (M. Ni)

Nomenclature

A area (cm^2)
c speed of light ($\mathrm{cm}\cdot\mathrm{s}^{-1}$)
C isobaric molar heat capacity ($\mathrm{J}\cdot\mathrm{mol}^{-1}\cdot\mathrm{K}^{-1}$)
D^{eff} effective diffusion coefficient ($\mathrm{cm}^2\cdot\mathrm{s}^{-1}$)
D_{k} Knudsen diffusion coefficient ($\mathrm{cm}^2\cdot\mathrm{s}^{-1}$)
$D_{\mathrm{A\text{-}B}}$ binary diffusion coefficient ($\mathrm{cm}^2\cdot\mathrm{s}^{-1}$)
d thickness (cm)
E photon's energy (J)
E_{g} band-gap of semiconductor (J)
E_{C} conduction band energy level (J)
E_{V} valence band energy level (J)
E_{fe} quasi-Fermi level of electrons (J)
E_{fh} quasi-Fermi level of holes (J)
$\dot{N}$ photon flux (cm^{-2})
$\dot{E}$ energy flux ($\mathrm{W}\cdot\mathrm{cm}^{-2}$)
e elementary positive charge (C)
F Faraday's constant ($\mathrm{C}\cdot\mathrm{mol}^{-1}$)
Δg molar Gibbs energy ($\mathrm{J}\cdot\mathrm{mol}^{-1}$)
Δh molar enthalpy change ($\mathrm{J}\cdot\mathrm{mol}^{-1}$)
$\hbar$ reduced Planck constant ($\mathrm{J}\cdot\mathrm{s}$)
$-\Delta\dot{H}$ enthalpy change (J)
J operating current density ($\mathrm{A}\cdot\mathrm{cm}^{-2}$)
J_{e} exchange current density ($\mathrm{A}\cdot\mathrm{cm}^{-2}$)
J_{L} limiting current density ($\mathrm{A}\cdot\mathrm{cm}^{-2}$)
K_{B} Boltzmann constant ($\mathrm{eV}\cdot\mathrm{K}^{-1}$)
L_{por} average pore radius (cm)
l_{v} phase change Latent heat of water ($\mathrm{J}\cdot\mathrm{mol}^{-1}$)
M molecular mass ($\mathrm{kg}\cdot\mathrm{mol}^{-1}$)
n number of electrons transferred in reaction
P power (W)
P^* power density ($\mathrm{W}\cdot\mathrm{cm}^{-2}$)
p_{j} partial pressure (atm)
q_{rad} thermal radiative heat flow (W)
q_{in}^* input heat flow per unit area ($\mathrm{W}\cdot\mathrm{cm}^{-2}$)
v special Fuller diffusion volume (cm^3)
R universal gas constant ($\mathrm{J}\cdot\mathrm{mol}^{-1}\cdot\mathrm{K}^{-1}$)
r resistance (Ω)
T temperature (K)
V voltage (V)
W_{act} activation energy level ($\mathrm{J}\cdot\mathrm{mol}^{-1}$)

Greek symbols

α resistance ratio
β area ratio
γ pre-exponential factor ($\mathrm{A}\cdot\mathrm{cm}^{-2}$)
μ electrochemical potential (J)
σ electric conductivity ($\mathrm{S}\cdot\mathrm{cm}^{-1}$)
δ Stefan-Boltzmann constant ($\mathrm{W}\cdot\mathrm{cm}^{-2}\cdot\mathrm{K}^{-4}$)
ε emissivity
ξ tortuosity
τ porosity
η efficiency

Subscript

a anode
act activation over-potential
b boiling point
c cathode
con concentration over-potential
E environment
e electrolyte
F fuel cell
i interconnect
I internal
j H_2, O_2, H_2O
L limit
lb lower-bound
leak leakage resistance
max maximum
ohm ohmic over-potential
P^* power density point
P represent photovoltaic cell
R represent thermoradiative cell
Rad radiative
ref reference
S short-circuit
T typical point

Abbreviations

SOFC solid oxide fuel cell
TEGC thermoelectric generator-cooler
TPV thermophotovoltaic
TR thermoradiative

	VTEC vacuum thermionic energy converter

1. Introduction

With the substantial increase in energy consumption, the traditional energy supply and utilization ways have become more difficult to meet the demands of economic and social developments [1]. Thus, distributed power systems pay an important role of the world's energy supply [2]. As emerging power supply devices, the chemical energy in the supplied fuel and oxidant into electricity can be converted into electricity by solid oxide fuel cells (SOFCs) [3]. The SOFCs can utilize various hydrocarbon fuels such as hydrogen, carbon monoxide, natural gas, and biomass gas. Due to the advantages of wide fuel adaptability, high energy conversion efficiency, low pollution, etc., SOFCs have broad application prospects in the fields of stationary electric power plants and mobile power sources such as marine power supply and transportation vehicle power supply. Importantly, due to the high temperature exhaust gas produced in the SOFC, there exists large potential to generate additional electricity and improve efficiency through energy cascade utilization [4]. The previous work reported that the high-grade waste heat produced in SOFC can be exploited to generate hydrogen by reforming natural gas [5]. On the other hand, the previous works demonstrated that the hybrid systems can be constructed by integrating the large-scale power machinery and thermodynamics cycles such as gas turbine [6, 7], Stirling heat engine [8], Brayton cycle [9], organic Rankine cycle [10], Braysson cycle [11] into the SOFC. Similarly, the hybrid systems can be established by coupling the SOFC with the small-scale energy conversion devices such as thermoelectric generator (TEG) [12], thermoelectric generator-cooler (TEGC) [13], vacuum thermionic energy converter (VTEC)-TEG [14], VTECs [15-18], and thermophotovoltaic (TPV) cells [19, 20]. In the above-mentioned hybrid systems, the area matching between the subsystems was analyzed to predict the peak power density. The influences of key parameters and factors on the system were discussed to provide a basis for the design and optimization of the system.

Unlike the conventional TPV cells, the p-n junction formed thermoradiative (TR) cell is operated at a medium temperature, in which the valence band electrons are thermally excited to the conduction band to form electron-hole pairs, meanwhile, the carriers' recombination occur in the carrier generation process [21, 22]. As the recombination rate is larger than the production rate, the emissions of the photons from the p-n junction are larger that the absorptions of the photons from the cold side, resulting a negative value between the quasi-Fermi levels of electrons and holes and a negative output voltage [23-26]. In order to achieve energy cascade utilization, researchers placed the TR cell on the back of the VTEC's anode to harness waste heat, thus realizing production of additional electricity and increase in energy conversion efficiency [27, 28]. Especially, Our previous work proposed a physical model of TR-PV coupled cells, in which the TR cell's emitted infrared photons can be absorbed by the PV cell to generate additional electricity, resulting in high thermal-to-electrical energy conversion efficiency [29]. Tervo *et. al.* [30] proposed a model of solar-powered TR-PV cells. Based on the theory of detailed balance, the limiting solar conversion efficiencies for fully concentrated sunlight and one sun were calculated. Considering the multiple irreversible energy losses, the efficiency of a realistic device is obtained. The theoretical analysis in above models are helpful for developing and investigating other hybrid systems such as intermediate-temperature SOFC driven TR-PV cells. This research gap as an objective is to be filled in present work, we conceptually proposed and theoretically studied a novel SOFC-TR-PV hybrid system to reduce the emissions of waste heat and achieve energy cascade utilization. The positive effects of back surface reflector and the negative effects of leakage resistance, irreversible heat transfers, and heat leak on the hybrid system are discussed. The peak power density and the maximum efficiency and the relevant work conditions are achieved through parametric optimal analysis. The obtained results are helpful for designing and optimizing the SOFC-TR-PV hybrid systems.

2. Model descriptions and working principle

The SOFC-TR-PV hybrid system consisting of an SOFC, a TR cell, and a PV cell is depicted in Fig. 1(a), where the SOFC contacts the TR cell through the material with high heat transfer coefficient, the TR and PV cells separated by a vacuum gap can exchange radiative heat flow q_{Rad}. Four basic components: fuel electrode (anode), air electrode (cathode), electrolyte, and interconnect are composed in the SOFC. The fuel is oxidized in the anode, while oxidant is reduced in the cathode. Both of anode and cathode contain catalysts that can accelerate the electrochemical reaction. Hydrogen (H_2) is continuously fed into the anode. The fuel gas firstly absorbed by the catalyst and then transported to the triple-phase boundary at the anode/electrolyte interface through the porous anode. Air is continuously supplied to the cathode, and the porous cathode surface adsorbs oxygen. Due to the catalysis of the cathode, O_2 obtains electrons to form O^{2-}. By means of chemical potential, O^{2-} firstly enters the oxygen ion conducting electrolyte, and then reacts with the fuel gas at the interface between the solid electrolyte and the anode. The lost electrons return to the cathode through the external loads, resulting electricity production. The TR and PV cells' band diagrams are presented in Fig. 1(b), where the III-V group p- and n- doped semiconductors are utilized to form the p-n junction, $\hbar\omega$ is the photon's energy, $\hbar$ is the reduced Planck constant, ω is the photon's angular frequency, E_{V} and E_{C} are the energy levels at the top of the valence band and bottom of the conduction band, and E_{fe} and E_{fh} are the quasi-Fermi levels of electrons and holes, whose difference $\left(E_{\mathrm{fe}}-E_{\mathrm{fh}}\right)$ corresponds to the operating voltage V multiplied by an elementary positive charge e [21]. As the hybrid system is in operation, the TR cell is operated at the temperature T_{R} above the PV cell's temperature T_{P}, meanwhile, the TR cell's radiative photons with energy above the PV cell's band-gap are absorbed to produce carriers [29, 30]. The TR cell delivers electricity with a negative bias, while the electrons generated in the PV cell transfers to external load to supply

electricity with a positive bias [29, 30]. In order to make the system operate at steady state, the high-temperature exhaust gas of the SOFC and the PV cell preheat the incoming fuel and air within the regenerator [12-14].

2.1. The power production and efficiency of an SOFC

The decrement in enthalpy of the chemical reaction $\mathrm{H_2}+\frac{1}{2}\mathrm{O_2}=\mathrm{H_2O}$ is equal to the hybrid system's input power, i.e.,

$$-\Delta\dot{H}=-\Delta h J_{\mathrm{F}} A_{\mathrm{F}}/(nF), \tag{1}$$

where J_{F} is the SOFC's operating current density. A_{F} is the effective electrode area. $n=2$ denotes the number of electrons transferred in chemical reaction. $F=9.65\times10^{4}\,\mathrm{C\cdot mol^{-1}}$ means the Faraday's constant. The molar enthalpy change Δh for electrochemical reaction is given by [31]

$$\Delta h=h_{298}^{0}+\int_{298}^{T_{\mathrm{b}}}C_{\mathrm{p,H_2O(L)}}dT+l_{\mathrm{v}}+\int_{T_{\mathrm{b}}}^{T_{\mathrm{F}}}C_{\mathrm{p,H_2O(g)}}dT-\int_{298}^{T_{\mathrm{b}}}C_{\mathrm{p,H_2}}dT-\frac{1}{2}\int_{298}^{T_{\mathrm{F}}}C_{\mathrm{p,O_2}}dT, \tag{2}$$

where h_{298}^{0} is the water's standard enthalpy. l_{v} stands for the latent heat of phase change in the water. The water's boiling temperature is T_{b}. The isobaric molar heat capacities $C_{\mathrm{p,O_2}}$, $C_{\mathrm{p,H_2}}$, $C_{\mathrm{p,H_2O(L)}}$, and $C_{\mathrm{p,H_2O(g)}}$ of the respective ideal gases as a function of temperature are valid by neglecting the interparticle interactions. Because the enthalpy change of steam depends on temperature and pressure, the value $\Delta h=-247172\,\mathrm{J\cdot mol^{-1}}$ is chosen under the conditions of $T_{\mathrm{F}}=873\,\mathrm{K}$ and $p=1$ atm [12, 32].

According to the Nernst equation, the thermodynamic potential V_{Nernst} is given by [7, 33, 34]

$$V_{\mathrm{Nernst}}=-\frac{\Delta g(T_{\mathrm{F}})}{nF}-\frac{RT_{\mathrm{F}}}{nF}\ln\left(\frac{p_{\mathrm{H_2O}}}{p_{\mathrm{H_2}}p_{\mathrm{O_2}}^{0.5}}\right), \tag{3}$$

where $R=8.314\,\mathrm{J\cdot mol^{-1}\cdot K^{-1}}$ is the universal gas constant. $\Delta g(T_{\mathrm{F}})$ means the temperature dependent molar Gibbs energy change under the standard atmospheric pressure. $p_{\mathrm{H_2}}$, $p_{\mathrm{O_2}}$, and $p_{\mathrm{H_2O}}$ denote the partial pressures of the hydrogen, oxygen, and water, respectively.

The ohmic over-potential V_{ohm} can be calculated as [15, 35]

$$V_{\text{ohm}} = J_{\text{F}}\left(\frac{d_{\text{a}}}{\sigma_{\text{a}}}+\frac{d_{\text{c}}}{\sigma_{\text{c}}}+\frac{d_{\text{e}}}{\sigma_{\text{e}}}+\frac{d_{\text{i}}}{\sigma_{\text{i}}}\right), \tag{4}$$

where $d_{\text{a}} = 5.0\times10^{-2}\,\text{cm}$, $d_{\text{c}} = 5.0\times10^{-3}\,\text{cm}$, $d_{\text{e}} = 1.0\times10^{-3}\,\text{cm}$, and $d_{\text{i}} = 3.0\times10^{-1}\,\text{cm}$ are the thicknesses of the anode, cathode, electrolyte, and interconnect. $\sigma_{\text{a}} = 9.5\times10^{5}T_{\text{F}}^{-1}\exp\left(-1150/T_{\text{F}}\right)$, $\sigma_{\text{c}} = \frac{4.2\times10^{5}}{T_{\text{F}}}\exp\left(-\frac{1200}{T_{\text{F}}}\right)$, $\sigma_{\text{e}} = 3.34\times10^{2}\exp\left(\frac{-10300}{T_{\text{F}}}\right)$, and $\sigma_{\text{i}} = \frac{9.3\times10^{4}}{T_{\text{F}}}\exp\left(\frac{-1100}{T_{\text{F}}}\right)$ are the electronic or ionic conductivities.

The activation over-potential V_{act} is expressed as [15, 34, 35]

$$V_{\text{act}} = \frac{RT_{\text{F}}}{F}\left[\sinh^{-1}\left(\frac{J_{\text{F}}}{2J_{\text{e,a}}}\right)+\sinh^{-1}\left(\frac{J_{\text{F}}}{2J_{\text{e,c}}}\right)\right], \tag{5}$$

where the exchange current densities $J_{\text{e,a}}$ and $J_{\text{e,c}}$ are, respectively, expressed as [7, 33]

$$J_{\text{e,a}} = \gamma_{\text{a}}\left(\frac{p_{\text{H}_2}}{p_{\text{ref}}}\right)\left(\frac{p_{\text{H}_2\text{O}}}{p_{\text{ref}}}\right)\exp\left(-\frac{W_{\text{act,a}}}{RT_{\text{F}}}\right) \tag{6}$$

and

$$J_{\text{e,c}} = \gamma_{\text{c}}\left(\frac{p_{\text{O}_2}}{p_{\text{ref}}}\right)^{0.25}\exp\left(-\frac{W_{\text{act,c}}}{RT_{\text{F}}}\right), \tag{7}$$

where γ_{a} and γ_{c} are the pre-exponential factors based on Arrhenius law, respectively. $W_{\text{act,a}}$ and $W_{\text{act,c}}$ denote the activation energy levels. p_{ref} means the reference partial pressure.

The concentration over-potential V_{con} can be calculated as [7, 34]

$$V_{\text{con}} = V_{\text{con,a}} + V_{\text{con,c}} = \frac{RT}{nF}\ln\left(\frac{1+J_{\text{F}}/J_{\text{L,H}_2\text{O}}}{1-J_{\text{F}}/J_{\text{L,H}_2}}\right)+\frac{RT}{nF}\ln\left(\frac{J_{\text{L,O}_2}}{J_{\text{L,O}_2}-J_{\text{F}}}\right), \tag{8}$$

where $J_{\text{L,H}_2\text{O}}$ and $J_{\text{L,H}_2}$ denote the limiting current densities of the anode. $J_{\text{L,O}_2}$ stands for the limiting current density of the cathode. The limited current densities are given by [7, 34]

$$J_{\text{L,H}_2\text{O}} = \frac{nFD_{\text{H}_2\text{O}}^{\text{eff}}}{RT_{\text{F}}d_{\text{a}}}\,p_{\text{H}_2\text{O}}, \tag{9}$$

$$J_{\mathrm{L,H_2}} = \frac{nFD_{\mathrm{H_2}}^{\mathrm{eff}}}{RT_{\mathrm{F}}d_{\mathrm{a}}}\, p_{\mathrm{H_2}}, \tag{10}$$

and

$$J_{\mathrm{L,O_2}} = \frac{nFD_{\mathrm{O_2}}^{\mathrm{eff}}}{RT_{\mathrm{F}}d_{\mathrm{c}}}\, p_{\mathrm{O_2}}, \tag{11}$$

where $D_{\mathrm{H_2O}}^{\mathrm{eff}}$ and $D_{\mathrm{H_2}}^{\mathrm{eff}}$ stand for the effective diffusion coefficients at the anode. $D_{\mathrm{O_2}}^{\mathrm{eff}}$ is the effective diffusion coefficient at the cathode. Based on the Chapman–Enskog and kinetic theories, the effective diffusion coefficients $D_{\mathrm{H_2O}}^{\mathrm{eff}}$, $D_{\mathrm{H_2}}^{\mathrm{eff}}$, and $D_{\mathrm{O_2}}^{\mathrm{eff}}$ can be determined by combining molecular diffusion and Knudsen diffusion mechanisms, i.e., the Bosanquet formulas [7, 34]

$$\frac{1}{D_{\mathrm{H_2O}}^{\mathrm{eff}}} = \frac{\xi_{\mathrm{a}}}{\tau_{\mathrm{a}}}\left(\frac{1}{D_{\mathrm{H_2-H_2O}}} + \frac{1}{D_{\mathrm{H_2O,k}}}\right), \tag{12}$$

$$\frac{1}{D_{\mathrm{H_2}}^{\mathrm{eff}}} = \frac{\xi_{\mathrm{a}}}{\tau_{\mathrm{a}}}\left(\frac{1}{D_{\mathrm{H_2-H_2O}}} + \frac{1}{D_{\mathrm{H_2,k}}}\right), \tag{13}$$

and

$$\frac{1}{D_{\mathrm{O_2}}^{\mathrm{eff}}} = \frac{\xi_{\mathrm{c}}}{\tau_{\mathrm{c}}}\left(\frac{1}{D_{\mathrm{O_2-N_2}}} + \frac{1}{D_{\mathrm{O_2,k}}}\right), \tag{14}$$

where ξ/τ is the ratio of tortuosity to porosity. $D_{\mathrm{H_2-H_2O}} = \dfrac{1.43\times10^{-7}T_{\mathrm{F}}^{1.75}}{M_{\mathrm{H_2-H_2O}}^{0.5}\left(\nu_{\mathrm{H_2}}^{1/3}+\nu_{\mathrm{H_2O}}^{1/3}\right)^2 p}$ and $D_{\mathrm{O_2-N_2}} = \dfrac{1.43\times10^{-7}T_{\mathrm{F}}^{1.75}}{M_{\mathrm{O_2-N_2}}^{0.5}\left(\nu_{\mathrm{O_2}}^{1/3}+\nu_{\mathrm{N_2}}^{1/3}\right)^2 p}$ represent the binary molecular diffusion coefficients for H_2–H_2O and O_2–N_2. $D_{\mathrm{O_2,k}} = \dfrac{L_{\mathrm{por}}}{3}\sqrt{\dfrac{8RT_{\mathrm{F}}}{\pi M_{\mathrm{O_2}}}}$, $D_{\mathrm{H_2O,k}} = \dfrac{L_{\mathrm{por}}}{3}\sqrt{\dfrac{8RT_{\mathrm{F}}}{\pi M_{\mathrm{H_2O}}}}$, and $D_{\mathrm{H_2,k}} = \dfrac{L_{\mathrm{por}}}{3}\sqrt{\dfrac{8RT_{\mathrm{F}}}{\pi M_{\mathrm{H_2}}}}$ are the Knudsen diffusion coefficients for O_2, H_2O, and H_2 gases. ν is the special Fuller diffusion volume. $L_{\mathrm{por}} = 1\times10^{-4}\,\mathrm{cm}$ is the average pore radius. $M_{\mathrm{H_2-H_2O}} = 2\left(M_{\mathrm{H_2}}{}^{-1} + M_{\mathrm{H_2O}}{}^{-1}\right)^{-1}$ and $M_{\mathrm{O_2-N_2}} = 2\left(M_{\mathrm{O_2}}{}^{-1} + M_{\mathrm{N_2}}{}^{-1}\right)^{-1}$ are the relative molecular masses.

Based on the above equations, the efficiency η_{F} and the electricity P_{F} of the SOFC are, respectively, presented as [13, 18]

$$\eta_{\mathrm{F}}=\frac{P_{\mathrm{F}}}{-\Delta\dot{H}} \tag{15}$$

and

$$P_{\mathrm{F}}=V_{\mathrm{F}}J_{\mathrm{F}}\left(1-\alpha V_{\mathrm{F}}/V_{\mathrm{loss}}\right), \tag{18}$$

where $\alpha=r_{\mathrm{I}}/r_{\mathrm{Leak}}$ is the ratio of the over-potentials caused internal resistance $r_{\mathrm{I}}=\left(V_{\mathrm{act}}+V_{\mathrm{con}}+V_{\mathrm{ohm}}\right)/\left(J_{\mathrm{F}}A_{\mathrm{F}}\right)$ to leakage resistance r_{Leak} in parallel with the load. $V_{\mathrm{F}}=V_{\mathrm{Nernst}}-V_{\mathrm{act}}-V_{\mathrm{con}}-V_{\mathrm{ohm}}$ denotes the SOFC's operating voltage. $V_{\mathrm{loss}}=V_{\mathrm{act}}+V_{\mathrm{con}}+V_{\mathrm{ohm}}$ is the total of voltage losses. The operating conditions and parametric choices the SOFC are presented in Table 1 [7, 36].

2.2. The electricity production of TR-PV cells

As the radiative photons' energies locate in the range of E_1 to E_2, the photon flux $\dot{N}$ and radiative heat flow $\dot{E}$ of photons with temperature T and electrochemical potential μ are calculated as [19, 21]

$$\dot{N}\left(E_1,E_2,T,\mu\right)=\frac{1}{4\pi^2\hbar^3c^2}\int_{E_1}^{E_2}\frac{E^2dE}{\exp\left[\left(E-\mu\right)/\left(K_{\mathrm{B}}T\right)\right]-1} \tag{17}$$

and

$$\dot{E}\left(E_1,E_2,T,\mu\right)=\frac{1}{4\pi^2\hbar^3c^2}\int_{E_1}^{E_2}\frac{E^3dE}{\exp\left[\left(E-\mu\right)/\left(K_{\mathrm{B}}T\right)\right]-1}, \tag{18}$$

where c is the speed of light. K_{B} is the Boltzmann's constant.

It is assumed that the thermal emissivities of the surfaces of the TR and PV cell are equal to 1, the principle of detailed balance can be to derive the electrical current densities J_{R} and J_{P}, i.e., [29, 30]

$$J_{\mathrm{R}}=\begin{cases}e\left[\dot{N}\left(E_{\mathrm{g,R}},E_{\mathrm{g,P}},T_{\mathrm{P}},0\right)+\dot{N}\left(E_{\mathrm{g,P}},\infty,T_{\mathrm{P}},eV_{\mathrm{P}}\right)-\dot{N}\left(E_{\mathrm{g,R}},\infty,T_{\mathrm{R}},eV_{\mathrm{R}}\right)\right], & \text{If } E_{\mathrm{g,R}}\le E_{\mathrm{g,P}}\\ e\left[\dot{N}\left(E_{\mathrm{g,R}},\infty,T_{\mathrm{P}},eV_{\mathrm{P}}\right)-\dot{N}\left(E_{\mathrm{g,R}},\infty,T_{\mathrm{R}},eV_{\mathrm{R}}\right)\right], & \text{If } E_{\mathrm{g,R}}>E_{\mathrm{g,P}}\end{cases} \tag{19}$$

and

$$J_{\mathrm{P}}=\begin{cases} e\left[\dot{N}\left(E_{\mathrm{g,P}},\infty,T_{\mathrm{R}},eV_{\mathrm{R}}\right)-\dot{N}\left(E_{\mathrm{g,P}},\infty,T_{\mathrm{P}},eV_{\mathrm{P}}\right)\right], & \text{If } E_{\mathrm{g,R}}\le E_{\mathrm{g,P}} \\ e\left[\dot{N}\left(E_{\mathrm{g,P}},E_{\mathrm{g,R}},T_{\mathrm{R}},0\right)+\dot{N}\left(E_{\mathrm{g,R}},\infty,T_{\mathrm{R}},eV_{\mathrm{R}}\right)-\dot{N}\left(E_{\mathrm{g,P}},\infty,T_{\mathrm{P}},eV_{\mathrm{P}}\right)\right], & \text{If } E_{\mathrm{g,R}}>E_{\mathrm{g,P}} \end{cases}, \quad (20)$$

where $E_{\mathrm{g,P}}$ and $E_{\mathrm{g,R}}$ are, respectively, the band-gaps of the PV and the TR cells. As III-V group semiconductor InAs is chosen to make the PV and TR cells, the dependences of the band-gaps $E_{\mathrm{g,R}}$ and $E_{\mathrm{g,P}}$ of the on the operating temperatures T_{R} and T_{P} are given by [37]

$$\frac{E_{\mathrm{g,R}}}{e}=0.42-\frac{0.28\times10^{-3}T_{\mathrm{R}}^{2}}{T_{\mathrm{R}}+93} \quad (21)$$

and

$$\frac{E_{\mathrm{g,P}}}{e}=0.42-\frac{0.28\times10^{-3}T_{\mathrm{P}}^{2}}{T_{\mathrm{P}}+93}, \quad (22)$$

where $E_{\mathrm{g,R}}<E_{\mathrm{g,P}}$ is satisfied due to $T_{\mathrm{R}}>T_{\mathrm{P}}$.

The power outputs P_{R} and P_{P} produced in the TR and the PV cells are given by

$$P_{\mathrm{R}}=V_{\mathrm{R}}J_{\mathrm{R}}A_{\mathrm{R}}, \quad (23)$$

and

$$P_{\mathrm{P}}=V_{\mathrm{P}}J_{\mathrm{P}}A_{\mathrm{P}}, \quad (24)$$

where the assumption $A_{\mathrm{R}}=A_{\mathrm{P}}$ is adopted.

Based on Eq. (18), the exchange heat q_{Rad} per unit time within the TR and PV cells are given by

$$q_{\mathrm{Rad}}=A_{\mathrm{R}}\left[\dot{E}\left(0,E_{\mathrm{g,R}},T_{\mathrm{R}},0\right)+\dot{E}\left(E_{\mathrm{g,R}},\infty,T_{\mathrm{R}},eV_{\mathrm{R}}\right)-\dot{E}\left(0,E_{\mathrm{g,P}},T_{\mathrm{P}},0\right)-\dot{E}\left(E_{\mathrm{g,P}},\infty,T_{\mathrm{P}},eV_{\mathrm{P}}\right)\right]. \quad (25)$$

2.3 The overall power production and efficiency of the hybrid system

By using Eqs. (1), (16), (23), and (24), the total electricity and overall efficiency of the SOFC-TR-PV hybrid system are derived as

$$P=P_{\mathrm{F}}+P_{\mathrm{R}}+P_{\mathrm{P}}=V_{\mathrm{F}}J_{\mathrm{F}}A_{\mathrm{F}}\left(1-\alpha V_{\mathrm{F}}/V_{\mathrm{loss}}\right)+A_{\mathrm{R}}\left(V_{\mathrm{R}}J_{\mathrm{R}}+V_{\mathrm{P}}J_{\mathrm{P}}\right) \quad (26)$$

and

$$\eta = \frac{P}{-\Delta \dot{H}} = \frac{V_{\mathrm{F}} J_{\mathrm{F}} \left(1 - \alpha V_{\mathrm{F}} / V_{\mathrm{loss}}\right) + \beta^{-1} \left(V_{\mathrm{R}} J_{\mathrm{R}} + V_{\mathrm{P}} J_{\mathrm{P}}\right)}{-\Delta h J_{\mathrm{F}} / \left(nF\right)}. \tag{27}$$

where $\beta = A_{\mathrm{F}} / A_{\mathrm{R}}$ is the area ratio of SOFC to TR cell.

3. Parametric optimization

3.1 Model validation

Fig. 2(a) shows the theoretical and experimental curves of the operating voltage and power density varying with the electrical current density, where the parametric selections are listed in Table 1 and kept constant in the next discussion unless specifically mentioned. Fig. 2(a) shows that the experimental data is smaller than modeling results in certain region, while the experimental data is larger than modeling results as the operating current density is close to the limit value.

As the TR cell is short-circuited, only the PV cell produces electricity. By considering the carriers' non-radiative recombination losses in the PV cell, the curves of the electrical current density varying with the operating voltage can be obtained to make comparisons between the present work and the reported work, as shown in Fig. 2(b). Because the previous work [21] has validated the model of TR cell, and the small discrepancy between the experimental and theoretical curves of the SOFC and the TPV is verified in Figs. 2(a) and (b), and thus, the subsystems' models can be applied to study the parametric optimal designs of the proposed hybrid system in present work.

3.2. The case of $\beta \geq 1$

Based on the first law of thermodynamics, an energy balance equation is written as

$$-\Delta \dot{H} - P_{\mathrm{F}} - \left(A_{\mathrm{F}} - A_{\mathrm{R}}\right)\left[U\left(T_{\mathrm{F}} - T_{\mathrm{E}}\right) + \varepsilon \delta \left(T_{\mathrm{F}}^4 - T_{\mathrm{E}}^4\right)\right] = q_{\mathrm{Rad}} + P_{\mathrm{R}}, \tag{28}$$

where $\left(A_{\mathrm{F}} - A_{\mathrm{R}}\right)\varepsilon \delta \left(T_{\mathrm{F}}^4 - T_{\mathrm{E}}^4\right)$ and $U\left(A_{\mathrm{F}} - A_{\mathrm{R}}\right)\left(T_{\mathrm{F}} - T_{\mathrm{E}}\right)$ are the radiative and the convective energy losses from the SOFC to the environment at temperature T_{E}. $\varepsilon = 0.05$ is the emissivity of the SOFC's surface. $\delta = 5.67 \times 10^{-12}\ \mathrm{W \cdot cm^{-2} \cdot K^{-4}}$ is the Stefan-Boltzmann constant.

$U = 5\times10^{-4}\,\mathrm{W\cdot cm^{-2}\cdot K^{-1}}$ is the natural convection coefficient.

Inserting Eqs. (1), (16), and (25) into Eq. (28), a new Equation can be obtained as

$$\beta\left[-\Delta h J_{\mathrm{F}}/(nF)-V_{\mathrm{F}}J_{\mathrm{F}}\right]-(\beta-1)\left[U(T_{\mathrm{F}}-T_{\mathrm{E}})+\varepsilon\delta\left(T_{\mathrm{F}}^4-T_{\mathrm{E}}^4\right)\right]=q_{\mathrm{in}}^*, \tag{29}$$

where $q_{\mathrm{in}}^* = (q_{\mathrm{Rad}}+P_{\mathrm{R}})/A_{\mathrm{R}}$ is the TR-PV cells' input heat flow per unit area.

Only in-equation $q_{\mathrm{in}}^*>0$ is satisfied, the TR and PV cells can convert the part of SOFC's waste heat into electricity. Neglecting the finite-time heat transfer from the SOFC to the TR cell, the TR cell's temperature T_{F} is equal to SOFC's temperature T_{R}. Varying the voltages V_{R} and V_{P}, the energy balance can be achieved by adjusting the area ratio β. Equation (29) is solved to determine the area ratio β for fixed parameters such as $J_{\mathrm{F}}=1.00\,\mathrm{A\cdot cm^{-2}}$, $T_{\mathrm{F}}=873\,\mathrm{K}$, etc. By Using Eq. (25), the 3D graph of q_{in}^* varying with V_{R} and V_{P} is plotted in Fig. 3(a). It is seen from Fig. 3(a) that q_{in}^* monotonically decay with $|V_{\mathrm{R}}|$ increases, while q_{in}^* firstly keeps a constant and then dramatically decreases as V_{P} increases. Because of a fixed J_{F}, the variations of q_{in}^* with V_{R} and V_{P} determine the variations of β with V_{R} and V_{P}, as verified in Fig. 3(b). Inserting the values of J_{F}, β, V_{R}, and V_{P} into Eqs. (26) and (27), the electricity $P^*=P/A_{\mathrm{F}}$ and efficiency η can be calculated. Figs. 3(c) and (d) reveal that the optimal power density $P_{\mathrm{opt}}^*=0.524\,\mathrm{W\cdot cm^{-2}}$ and the optimal efficiency $\eta_{\mathrm{opt}}=0.410$ can be achieved under the similar optimal conditions of $V_{\mathrm{R}}=V_{\mathrm{R,opt}}=-0.0659\,\mathrm{V}$ and $V_{\mathrm{P}}=V_{\mathrm{P,opt}}=0.191\,\mathrm{V}$. By using $V_{\mathrm{R,opt}}$ and $V_{\mathrm{P,opt}}$, the optimal area ratio $\beta_{\mathrm{opt}}=2.30$ can be calculated. Varying the electrical current density J_{F}, the optimal values P_{opt}^* and η_{opt} change accordingly, as shown in Fig. 4(a). What's more, the numerical simulation reveal that β_{opt} closely depends on J_{F}, while $V_{\mathrm{R,opt}}$ and $V_{\mathrm{P,opt}}$ change negligibly as J_{F} is increased. Thus, the global optimization of the electrical and structure parameters are great of importance for the hybrid system. In next section, we will discuss above key issue.

3.3. The case of $\beta<1$

As $\beta < 1$ is satisfied, Eq. (29) can be rewritten as

$$\beta\left[-\Delta h J_{\mathrm{F}}/(nF)-V_{\mathrm{F}}J_{\mathrm{F}}\right]=q_{\mathrm{in}}^{*}. \tag{30}$$

For given the electrical current density J_{F}, the optimal values P_{opt}^{*} and η_{opt} can be similarly obtained, as depicted in Figs. 4(a) and (b). In Fig. 4(a), we define a typical point $J_{\mathrm{F,T}}$ at which the area ratio β is equal to 1. Eq. (29) is adopted to analysis the system in the region of $J_{\mathrm{F}} < J_{\mathrm{F,T}}$; Eq. (30) is adopted to analysis the system in the region of $J_{\mathrm{F}} \geq J_{\mathrm{F,T}}$. In order to make comparisons between the single SOFC and the hybrid system, the SOFC's power density $P_{\mathrm{F}}^{*}=P_{\mathrm{F}}/A_{\mathrm{F}}$ and the efficiency η_{F} are plotted in Figs. 4(a) and (b) , respectively. It is seen from Fig. 4(a) that only the SOFC can produce electricity in the region of $J_{\mathrm{F}} \leq J_{\mathrm{F,lb}}$, while the power density and efficiency of the hybrid system can surpass those of the SOFC as the current density locates in the region of $J_{\mathrm{F}} > J_{\mathrm{F,lb}}$, where $J_{\mathrm{F,lb}}$ is defined as a lower-bound electrical current density. Figs. 4(a) and (b) show that P_{opt}^{*} achieves its maximum value $P_{\mathrm{max}}^{*}=0.670\,\mathrm{W\cdot cm^{-2}}$ at $J_{\mathrm{F}}=J_{\mathrm{F},P^{*}}=1.24\,\mathrm{A\cdot cm^{-2}}$, while η_{opt} achieves its maximum value $\eta_{\mathrm{max}}=0.770$ at $J_{\mathrm{F}}=J_{\mathrm{F},\eta}=0.170\,\mathrm{A\cdot cm^{-2}}$. Because of the irreversible thermal losses within the electrochemical process in SOFC, and thus, the peak values P_{max}^{*} and η_{max} are obtained at different current densities, i.e., $J_{\mathrm{F},P^{*}} > J_{\mathrm{F},\eta}$. By optimizing J_{F}, the SOFC's peak points $P_{\mathrm{F,max}}^{*}=0.528\,\mathrm{W\cdot cm^{-2}}$ and $\eta_{\mathrm{F,max}}=0.727$ can be obtained. The calculated results $\left(P_{\mathrm{max}}^{*}-P_{\mathrm{F,max}}^{*}\right)/P_{\mathrm{F,max}}^{*}=26.7\%$ and $\left(\eta_{\mathrm{max}}-\eta_{\mathrm{F,max}}\right)/\eta_{\mathrm{F,max}}=5.58\%$ indicate that the improvement of power output density is remarkable, while the improvement of efficiency is too small. Because the waste heat flow $\left(-\Delta\dot{H}-P_{\mathrm{F}}\right)$ is a monotonic increasing function of J_{F}, the small value $\left(-\Delta\dot{H}-P_{\mathrm{F}}\right)$ under the condition $J_{\mathrm{F}}=J_{\mathrm{F},\eta}$ leads that the addiational electricity produced by TR-PV cells is too small. As we increase J_{F} from $J_{\mathrm{F,T}}$ to the short-circuit current density $J_{\mathrm{F,S}}=2.04\,\mathrm{A\cdot cm^{-2}}$, the optimal power density P_{opt}^{*} decreases montically as J_{F} increases. Because the main electricity

generated in the hybrid system is supplied by the SOFC, the variation P_{F}^{*} with J_{F} determines the curve $J_{\mathrm{F}} \sim P_{\mathrm{opt}}^{*}$ in the region of $J_{\mathrm{F,T}} \le J_{\mathrm{F}} \le J_{\mathrm{F,S}}$. Numerical simulation results uncover that P_{opt}^{*} and η_{opt} simultaneously occur at similar area ratio β_{opt}. Fig. 4(c) shows that the optimized area ratio β_{opt} is a monotonic decreasing function of J_{F}. The inset presents the curves of the P_{opt}^{*} and η_{opt} varying with β_{opt}, where $\beta_{P^{*}} = 1.89$ and $\beta_{\eta} = 34.7$ are, respectively, the area ratios at P_{max}^{*} and η_{max}.

Using the data in Figs. 4(a) and 4(b), the performance characteristic curve of P^{*} as a function of η is plotted in Fig. 4(d). Generally, the negative slope part in Fig. 3(d) is depicted when J_{F} locates in the region of:

$$J_{\mathrm{F},\eta} \le J_{\mathrm{F}} \le J_{\mathrm{F,P^{*}}}. \tag{31}$$

Based on the above region, the optimal regions of power density P^{*} and the efficiency η can be determined as:

$$P_{\mathrm{max}}^{*} \ge P^{*} > P_{\eta}^{*} \tag{32}$$

and

$$\eta_{\mathrm{max}} \ge \eta \ge \eta_{\mathrm{P^{*}}}, \tag{33}$$

where P_{η}^{*} and $\eta_{\mathrm{P^{*}}}$ are, respectively, the power density and the efficiency at $\eta = \eta_{\mathrm{max}}$ and $P^{*} = P_{\mathrm{max}}^{*}$. In above regions, the hybrid system can exhibit high performances.

3.4. The effects of leakage resistance

The effects of the resistance ratio α on the hybrid system are presented in Fig. 4. One can find in Fig. 5 that decreasing the resistance ratio α, i.e., the SOFC's leakage resistance r_{I} can improve the hybrid system's performances. It is seen from Fig. 4 that β_{η}, P_{max}^{*}, $\eta_{P^{*}}$, and η_{max} monotonically decrease as α increases, while $\beta_{P^{*}}$, $J_{\mathrm{F},P^{*}}$, $J_{\mathrm{F},\eta}$, and P_{η}^{*} are monotonically increasing functions of α. The above results are restricted by the energy balance equations. The Joule heat generated in the

SOFC increases as α is increased, which leads that. It is found from Fig. 5 that the optimal regions $\left(P_{\max}^{*}-P_{\eta}^{*}\right)$, $\left(\eta_{\max}-\eta_{P^{*}}\right)$, $\left(J_{\mathrm{F},P^{*}}-J_{\mathrm{F},\eta}\right)$, and $\left(\beta_{\eta}-\beta_{P^{*}}\right)$ decrease with increasing of α.

3.5. The effects of materials selections

The influences of the semiconductor materials selections on the parametric optimal characteristics of the system are listed in Table 2, where the band-gaps of the following semiconductors varying with temperature are obtained from Ref. [37], two homo-structures: InAs-InAs and GaSb- GaSb and four hetero-structures: InAs-InSb, InAs-GaSb, GaSb-InAs, and GaSb-InSb are designed for constructing the SOFC-TR-PV hybrid system. Note that homo-structure: InSb-InSb and hetero-structures: InSb-InAs and InSb-GaSb aren't chosen for making the hybrid system due to the SOFC's operating temperature 873 K surpass the Indium Antimonide's boiling point 800 K. Comparing the maximum power densities and maximum efficiencies in Table 2, the optimum structure: GaSb-InSb is determined. In addition, Table 2 shows that the optimal electrical current density $J_{\mathrm{F},\eta}$ keeps at a constant. Because the SOFC provides the most of electricity at the hybrid system's maximum efficiency point, and thus, the semiconductor materials selections have negligible effects on $J_{\mathrm{F},\eta}$. Importantly, the compound semiconductor $In_xGa_{1-x}As_ySb_{1-y}$ can be selected to make the TR and PV cells, the performances of the SOFC-TR-PV system may be further improved. In the future, the variations of E_{g} with the operating temperature and the components: x and y should be determined to investigate the structure optimum design for the TR-PV cells.

3.6. The effects of back surface reflector

As back surface reflector is placed on the PV cell, the sub-bandgap photons stimulated from the TR cell can't contribute the radiative heat exchange [40]. Based on above assumption, Eq. (25) can be rewritten as

$$q_{\mathrm{Rad}} = A_{\mathrm{R}}\left[\dot{E}\left(E_{\mathrm{g,R}},\infty,T_{\mathrm{R}},eV_{\mathrm{R}}\right)-\dot{E}\left(E_{\mathrm{g,R}},E_{\mathrm{g,P}},T_{\mathrm{P}},0\right)-\dot{E}\left(E_{\mathrm{g,P}},\infty,T_{\mathrm{P}},eV_{\mathrm{P}}\right)\right]. \tag{34}$$

The performances comparisons can be made under the conditions of the existence and non-existence of back surface reflector. Based on the optimum structure GaSb-InSb of the TR-PV cells and the back surface reflector, the peak values $P_{\max}^{*}=1.05\,\mathrm{W\cdot cm^{-2}}$ and $\eta_{\max}=0.835$ and the corresponding parametric conditions can be obtained, as shown in Table 3. Comparing the values $P_{\max}^{*}$ and $\eta_{\max}$ in Table 3 to those values in Table 2, one can find that both of power density and efficiency are significantly enhanced. Because q_{Rad} is decreased by means of back surface reflector, selecting small area ratio can meet the energy balance equation at the maximum power density point, and thus, the result $\beta_{P^{*}}<1$ occurs. However, the result $\beta_{\eta}>1$ occurs, because the SOFC' waste heat production at the system's maximum efficiency point is very small, the energy balance equation needs large area ratio to meet. In addition, it is should be point that the irreversible heat transfers at the interfaces have negative influences on the hybrid system. The above key issue is discussed in next section.

As heat transfers at the hot and cold sides in the system obey Newton's cooling law, q_{in} and q_{out} are given by

$$q_{\mathrm{in}}=\begin{cases}U_{\mathrm{in}}A_{\mathrm{F}}\left(T_{\mathrm{F}}-T_{\mathrm{R}}\right) & \text{If } \beta\le 1\\ U_{\mathrm{in}}A_{\mathrm{F}}\left(T_{\mathrm{F}}-T_{\mathrm{R}}\right) & \text{If } \beta>1\end{cases} \tag{35}$$

and

$$q_{\mathrm{out}}=U_{\mathrm{out}}A_{\mathrm{R}}\left(T_{\mathrm{P}}-T_{\mathrm{E}}\right), \tag{36}$$

where $U_{\mathrm{in}}=10^{-2}\,\mathrm{W\cdot cm^{-2}\cdot K^{-1}}$ and $U_{\mathrm{out}}=10^{-2}\,\mathrm{W\cdot cm^{-2}\cdot K^{-1}}$ are the heat transfer coefficients.

Based the non-ideal vacuum environment within the TR-PV cells, the convection heat loss can be defined as

$$q_{\mathrm{Loss}}=U_{\mathrm{Loss}}A_{\mathrm{R}}\left(T_{\mathrm{R}}-T_{\mathrm{P}}\right), \tag{37}$$

where $U_{\mathrm{Loss}} = 10^{-6}\,\mathrm{W\cdot cm^{-2}\cdot K^{-1}}$ is the convective coefficient within the TR-PV cells.

For given relevant parameters, the area ratio β and temperatures T_{R} and T_{P} can be obtained by solving energy balance equations. According to multi-objective optimization of parameters, the peak values $P_{\max}^{*} = 0.875\,\mathrm{W\cdot cm^{-2}}$ and $\eta_{\max} = 0.772$ and the corresponding parametric conditions are determined in Table 3. The results in Table indicate that the selection of thermal conduction material with high heat transfer coefficients are of great importance for the hybrid system. It should be pointed out that only the medium temperature SOFCs is suitable for driving the TR-PV cells due to the III-V group semiconductor materials' thermal properties. The compound semiconductors $In_xGa_{1-x}As_ySb_{1-y}$ formed by InSb, InAs, and GaSb can be selected to make the TR and the PV cells, the performance of the SOFC-TR-PV hybrid system can be further enhanced via materials' band-gap optimization.

Fig. 6 shows that the peak power point obtained in the present work is larger than those of other hybrid energy systems such as SOFC-TPV, SOFC-TEGC, SOFC-TEG, etc., while it is smaller than that of a SOFC-VTEC, as the SOFC operated at high-temperature 1073 K and the VTEC's electricity production enhanced by novel two-dimensional material graphene.

5. Conclusions

An energy cascade utilization hybrid system has been conceptually constructed and theoretically studied. The obtained results are presented as follows:

(1) As semiconductor Indium Arsenide (InAs) is chosen to make the homo-structure of TR-PV cells, the peak values $P_{\max}^{*} = 0.669\,\mathrm{W\cdot cm^{-2}}$ and $\eta_{\max} = 0.770$ are achieved through energy balance analysis, area matching, and parametric optimal designs. Making trades-off between electricity and efficiency, the parametric optimal regions are provided.

(2) The effects of the resistance ratio α on the optimal performances of the system are discussed. The results reveal that decreasing SOFC's leakage resistance can improve the performances of the

hybrid system.

(3) The influences of semiconductor selections on the optimal performances of the system are assessed. The optimum structure: GaSb-InSb of the TR-PV cells is determined to improve the system's electricity production and energy conversion efficiency.

(4) The positive effect of back surface reflector and negative effect of irreversible heat transfers on the hybrid system are revealed.

The obtained results in present work can provide a theoretical basis for the optimal designs and energy management strategies of various types of novel fuel cell hybrid power generation systems.

Acknowledgements

This work has been supported by the Scientific Research Foundation (Grant No. 2019ZD22) and the Teaching Reform and Practice Project (Grant No. 2020YB29) of Chongqing University of Technology, the Science and Technology Research Program of Chongqing Municipal Education Commission (Grant No. KJQN201901144), and the Chongqing Research Program of Basic Research and Frontier Technology (cstc2020jcyjmsxmX0001), People's Republic of China. M. Ni thanks the grant (Project ID: P0014036; Work Programme: YW3T) from The Hong Kong Polytechnic University, Hong Kong, China.

References

[1] M. Shahbaz, C. Raghutla, K.R. Chittedi, Z. Jiao, X.V. Vo, Energy 207 (2020) 118162.

[2] S. Kang, K. Y. Ahn, Appl. Energy 195 (2017) 1086–1099.

[3] X. J. Luo, K. F. Fong, J. Power Sources 429 (2019) 127–148.

[4] X. Yang, H. Zhao, Energy 186 (2019) 115860.

[5] G. Benveniste, M. Pucciarelli, M. Torrell, M. Kendall, A. Tarancón, J. Clean Prod. 165 (2017) 312–322.

[6] X. Ding, X. Lv, Y. Weng, Appl. Energy 254 (2019) 113675.

[7] Y. Huang, A. Turan, Appl. Energy 283 (2021) 116237.

[8] H. Xu, B. Chen, P. Tan, H. Zhang, J. Yuan, J. Liu, M. Ni, Energy 140 (2017) 979–987.

[9] Z. Yang, H. Zhang, M. Ni, B. Lin. Appl. Therm. Eng. 160 (2019) 113992.

[10] F. A. Al-Sulaiman, I. Dincer, F. Hamdullahpour, J. Power Sources 195 (2010) 2346–2354.

[11] X. Chen, B. Lin, J. Chen, Energy Fuels 23 (2009) 6079–6084.

[12] X. Chen, Y. Pan, J. Chen, Fuel Cell 10 (2010) 1164–1170.

[13] H. Zhang, W. Kong, F. Dong, H. Xu, B. Chen, M. Ni, Energy Convers. Manage. 148 (2017) 1382–1390.

[14] S. Chen, H. Zhang, F.. Wang, H. Miao, J. Zhao, C. Zhang, J. Yuan, Int. J. Hydrogen Energy 46 (2021) 22062–22078.

[15] H. Zhang, J. Wang, F. Wang, J. Zhao, H. Miao, J. Yuan, Energy Convers. Manage. 193 (2019) 64–73.

[16] H. Xu, B. Chen, P. Tan, W. Cai, Y. Wu, H. Zhang, M. Ni, Appl. Energy 226 (2018) 881–890.

[17] T. Liao, Y. Dai, C. Cheng, Q. He, M. Ni. J. Power Sources 478 (2020) 228797.

[18] Y. Wang, L. Cai, T. Liu, J. Wang, Chen J, Energy 93 (2015) 900–907.

[19] T. Liao, L. Cai, Y. Zhao, J. Chen, J. Power Sources 306 (2016) 666–673.

[20] T. Liao, Q. He, Q. Xu, Y. Dai, C. Cheng, M. Ni, J. Power Sources 452 (2020) 227831.

[21] R. Strandberg, J. Appl. Phys. 117 (2015) 055105.

[22] P. Santhanam, S. Fan, Phys. Rev. B 93 (2016) 161410.

[23] J. J. Fernández, J. Appl. Phys. 123 (2018) 164501.

[24] T. Liao, X. Zhang, B. Lin, X. Chen, J. Chen, Opt. Lett. 42 (2017) 3236.

[25] J. J. Fernández, IEEE Trans. Electron Devices 64 (2017) 250.

[26] X. Zhang, W. Peng, J. Lin, X. Chen, J. Chen, J. Appl. Phys. 122 (2017) 174505.

[27] T. Liao, Y. Chen, Z. Yang, Sci. Sin. Tech. 51 (2021) 46–54.

[28] X. Zhang, Y. S. Ang, J. Y. Du, J. Chen. J. Cleaner Production 242 (2020) 118444.

[29] T. Liao, Z. Yang, X. Chen, J. Chen, IEEE Trans. Electron Devices 66 (2019) 1386–1389.

[30] E. J. Tervo, W. A. Callahan, E. S. Toberer, M. A. Steiner, A. J. Ferguson. Cell Rep. Phys. Sci. 1 (2020) 100258.

[31] J. Larminie, A. Dicks, Fuel Cell Systems Explained. New York: Wiley, 2000.

[32] Z. Yang, T. Liao, B. Lin. Sci Sin-Phys Mech Astron 44 (2014) 569–580.

[33] Z. Wu, P. Zhu, J. Yao, P. Tan, H. Xu, B. Chen, F. Yang, Z. Zhang, E. Porpatham, M. Ni. eTransportation 5 (2020) 100074.

[34] Z. Lyua, H. Menga, J. Zhua, M. Han, Z. Sun, H. Xue, Y. Zhao, F. Zhang, Appl. Energy 270 (2020) 115220.

[35] M. A. Haghghi, S. G. Holagh, A. Chitsaz, K. Parham, Energy Convers. Manage. 197 (2019) 111895.

[36] Q. Xu, L. Xia, Q. He, Z. Guo, M. Ni. Appl. Energy 291 (2021) 116832.

[37] J.A. Gonzalez-Cuevas, T.F. Refaat, M. Nurul Abedin, H.E. Elsayed-Ali, J. Appl. Phys. 102 (2007) 014504.

[38] Y. Zhang, B. Chen, D. Guan, M. Xu, R. Ran, M. Ni, Wei Zhou, R. O'Hayre, Z. Shao, Nature 591, (2021) 246–251.

[39] W. Xu, Y. Liu, L. Tang, Y. Zhang, C. Xu, Infrared Physics & Technology 115, (2021) 103719.

[40] V.P. Khvostikov, Ya.V. Grachev, A.S. Vlasov, O.A. Khvostikova, S.V. Sorokina, J. Power Sources 501 (2021) 229972.

List of Tables

List of Figures

Table 1. The operating conditions and parameters of the SOFC [7, 36].

Parameter	Value
Fuel composition pressures, p_{H_2} (atm); p_{H_2O} (atm)	0.97; 0.03
Air composition pressures, p_{O_2} (atm); p_{N_2} (atm)	0.21; 0.79
Cathode and anode exchange current densities, γ_c; γ_a ($A \cdot cm^{-2}$)	2.15×10^{11}; 5.59×10^{10}
Activation energy levels, $W_{act,a}$; $W_{act,c}$ ($J \cdot mol^{-1}$)	1.0×10^{5}; 1.37×10^{5}
Special Fuller diffusion volumes, ν_{H_2}; ν_{H_2O}; ν_{O_2} (cm^3)	6.12; 13.1; 16.3
Tortuosity, ξ	3
Porosity, τ	0.30

Table 2. The effects of semiconductor selections on the hybrid system, where $\alpha = 0.01$.

TR cell	PV cell	$P^{*}_{\max}\left(\mathrm{W}\cdot\mathrm{cm}^{-2}\right)$	$J_{\mathrm{F},P^{*}}\left(\mathrm{A}\cdot\mathrm{cm}^{-2}\right)$	$\beta_{P^{*}}$	$\eta_{\max}$	$J_{\mathrm{F},\eta}\left(\mathrm{A}\cdot\mathrm{cm}^{-2}\right)$	β_{η}
InAs	InAs	0.670	1.24	1.89	0.770	0.170	34.7
InAs	InSb	0.800	1.77	1.85	0.798	0.170	43.1
InAs	GaSb	0.618	1.15	1.76	0.756	0.170	28.3
GaSb	GaSb	0.534	1.01	4.07	0.730	0.170	52.5
GaSb	InAs	0.632	1.18	3.39	0.760	0.170	52.8
GaSb	InSb	0.812	1.48	1.73	0.800	0.170	43.1

Table 3. The effects of back surface reflector and Newton heat transfer on the hybrid system, where $\alpha = 0.01$.

Two Cases	$P^*_{\max}\left(\mathrm{W}\cdot\mathrm{cm}^{-2}\right)$	$J_{\mathrm{F},P^*}\left(\mathrm{A}\cdot\mathrm{cm}^{-2}\right)$	β_{P^*}	$\eta_{\max}$	$J_{\mathrm{F},\eta}\left(\mathrm{A}\cdot\mathrm{cm}^{-2}\right)$	β_η
Presence of back surface reflector	1.05	1.88	0.670	0.835	0.170	26.6
Presences of back surface reflector and Newton heat transfers	0.875	1.59	0.320	0.772	0.225	16.2

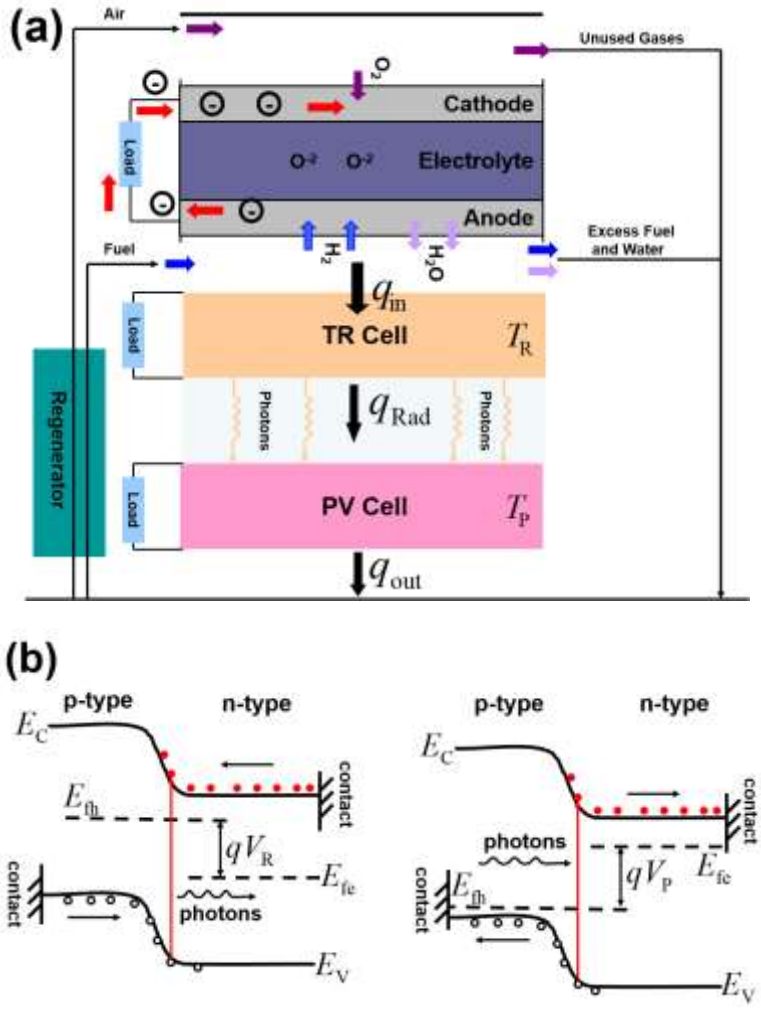

Fig. 1. (a) The schematic diagram of a SOFC-TR-PV hybrid system and (b) the band diagrams of a TR cell and a PV cell [27, 28].

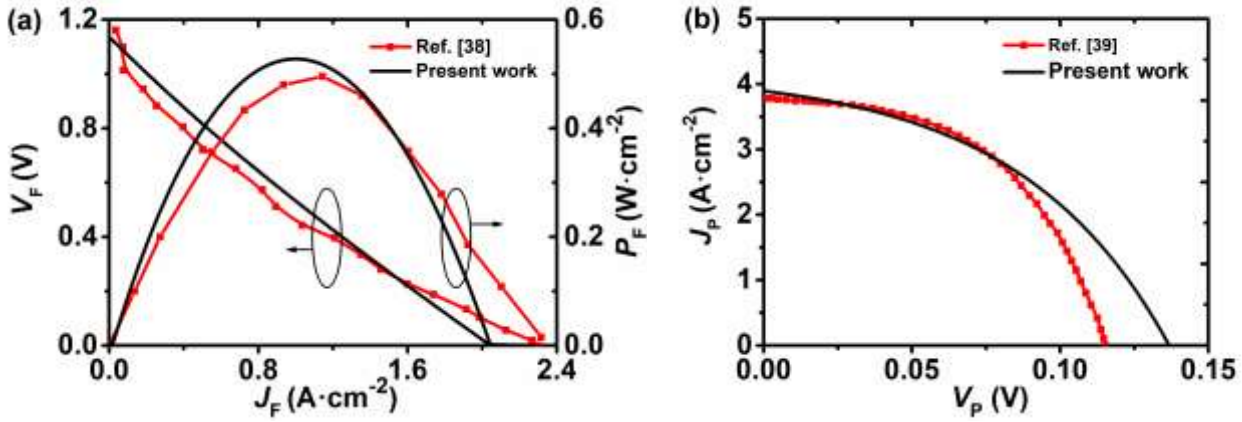

Fig. 2. (a) Comparison between the SOFC's theoretical results and the experimental data from Ref. [38] and (b) comparison between the InAs-based TPV's theoretical results and the reported data from Ref. [39], where $T_{\mathrm{p}} = 1073\mathrm{K}$ is chosen.

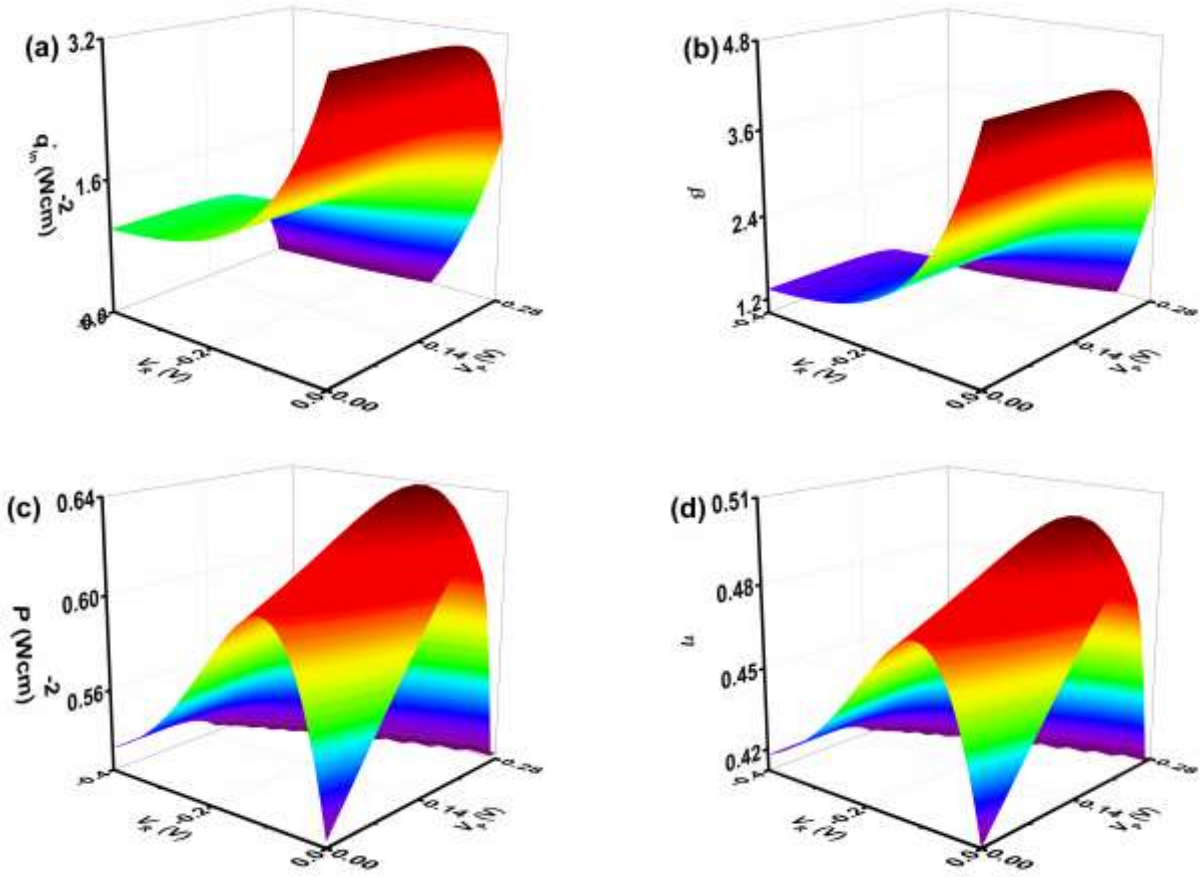

Fig. 3. The 3D graphs of (a) heat flow per unit area q_{in}^{*}, (b) area ratio β, (c) power density P^{*}, and (d) efficiency η varying with V_{R} and V_{P}, where $\alpha = 0.01$ and $T_{\text{F}} = 873\text{K}$ are chosen.

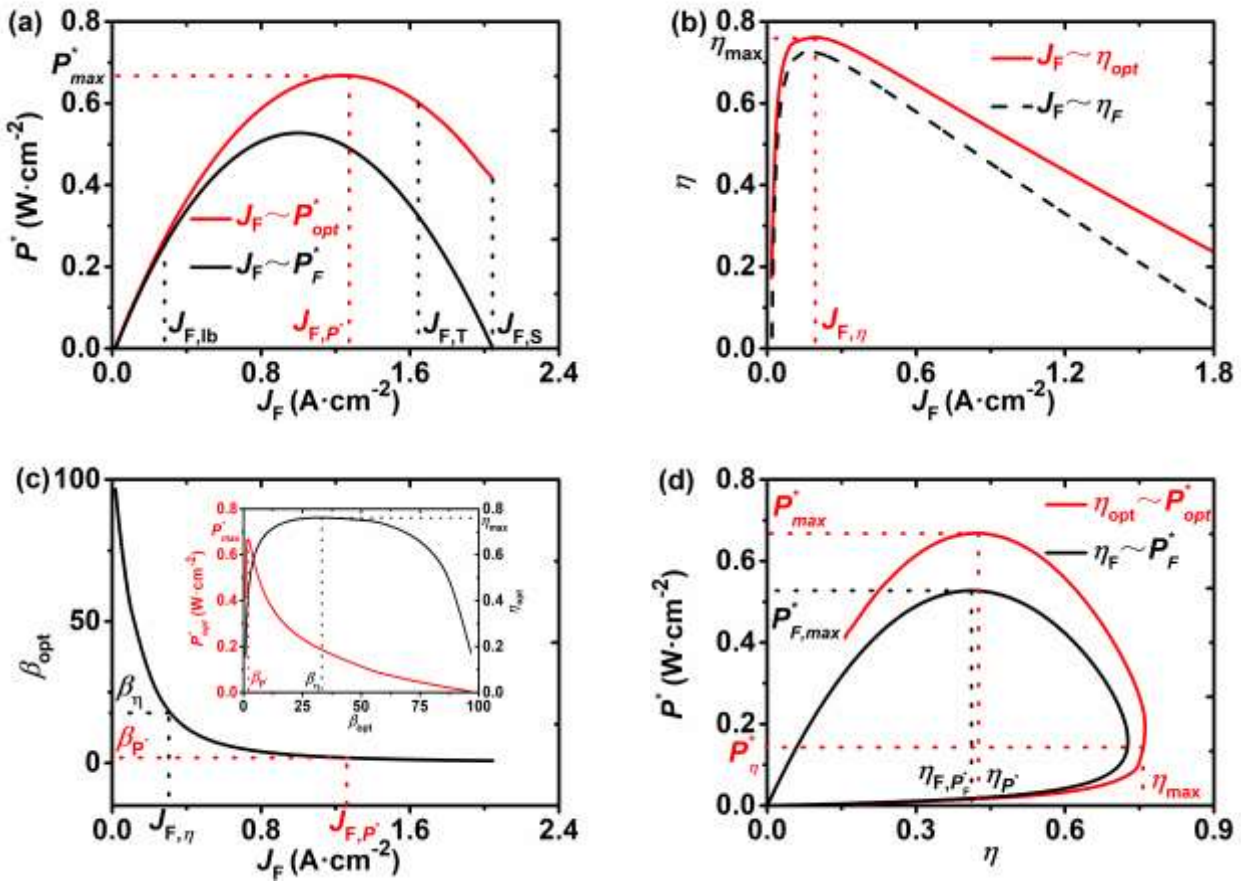

Fig. 4. The curves of (a) the optimal power density $P^*_{\rm opt}$ of the hybrid system and the power density $P^*_{\rm F}$ of the SOFC, (b) the optimal efficiency $\eta_{\rm opt}$ of the hybrid system and the efficiency $\eta_{\rm F}$ of the SOFC, (c) the optimal area ratio $\beta_{\rm opt}$ varying with the electrical current density $J_{\rm F}$, and (d) the performance characteristics curves of $\eta_{\rm opt} \sim P^*_{\rm opt}$ and $\eta_{\rm F} \sim P^*_{\rm F}$.

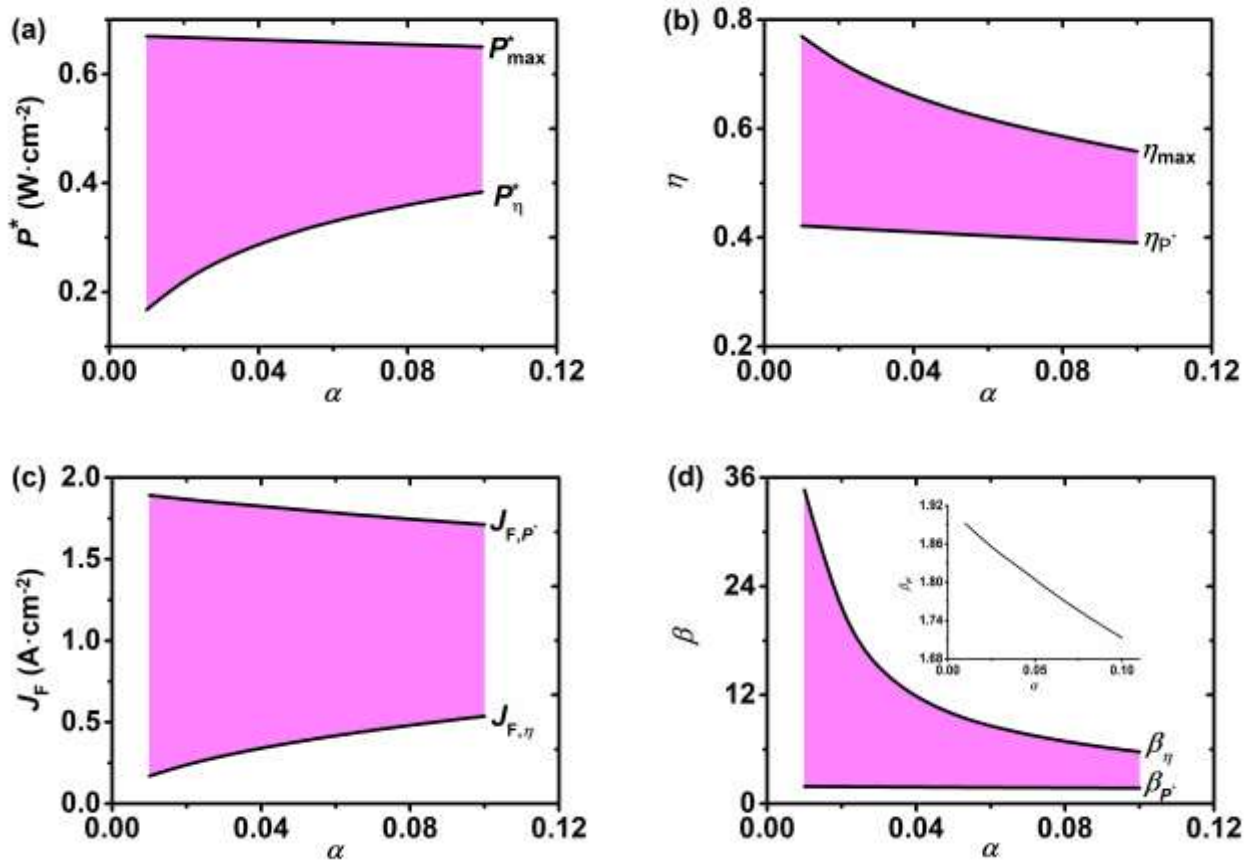

Fig. 5. The curves of (a) the optimal power densities P^*_{max} and P^*_{η}, (b) the optimal efficiencies η_{max} and η_{P^*}, (c) electrical current densities J_{F,P^*} and J_{η}, and (d) area ratios β_{P^*} and β_{η} varying with resistance ratio α.

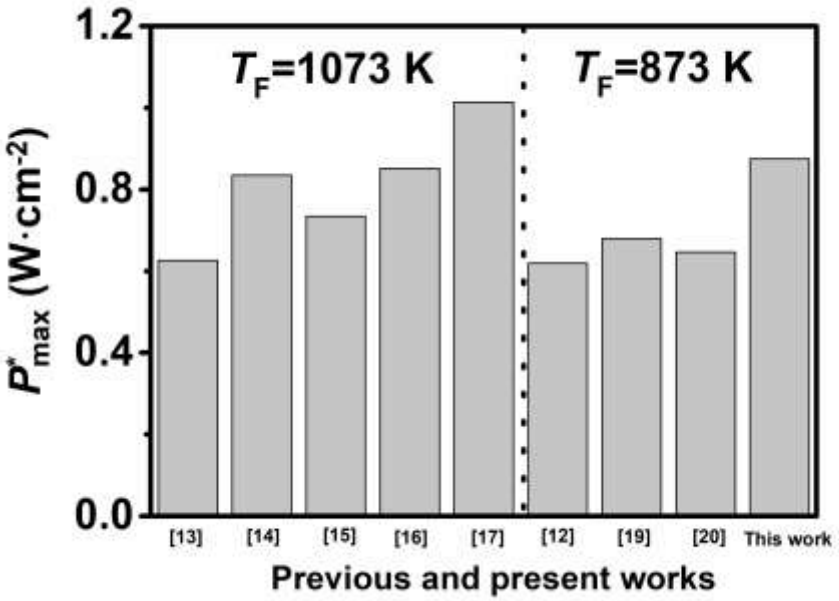

Fig. 6. the peak power points comparisons between the present work and other existing hybrid energy systems.